ACS Photonics

Article

pubs.acs.org/journal/apchd5

Transient Negative Optical Nonlinearity of Indium Oxide Nanorod Arrays in the Full-Visible Range

Peijun Guo,[†] Robert P. H. Chang,[*,‡] and Richard D. Schaller[*,†,§]

[†]Center for Nanoscale Materials, Argonne National Laboratory, 9700 South Cass Avenue, Lemont, Illinois 60439, United States

[‡]Department of Materials Science and Engineering, Northwestern University, 2220 Campus Drive, Evanston, Illinois 60208, United States

[§]Department of Chemistry, Northwestern University, 2145 Sheridan Road, Evanston, Illinois 60208, United States

Supporting Information

ABSTRACT: Dynamic control of the optical response of materials at visible wavelengths is key to future metamaterials and photonic integrated circuits. Materials such as transparent conducting oxides have attracted significant attention due to their large optical nonlinearity under resonant optical pumping condition. However, optical nonlinearities of TCOs are positive in sign and are mostly in the ε-near-zero to metallic range where materials can become lossy. Here we demonstrate large amplitude, negative optical nonlinearity (Δn from -0.05 to -0.09) of indium oxide nanorod arrays in the full-visible range where the material is transparent. We experimentally quantify and theoretically calculate the optical nonlinearity, which arises from a strong modification of interband optical transitions. The approach toward negative optical nonlinearity can be generalized to other transparent semiconducting oxides and opens door to reconfigurable, subwavelength optical components.

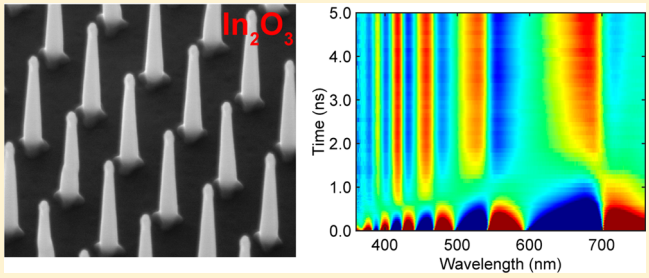

KEYWORDS: *indium oxide, transparent semiconducting oxide, negative optical nonlinearity, transient, ultrafast, full-visible range*

The development of miniaturized optical components necessitates strong nonlinear optical response of materials for active modulation and switching of optical signals at the nanoscale. Optical nonlinearity typically requires strong optical intensity and can arise from a variety of mechanisms. For example, the Kerr optical nonlinearity arising from the third-harmonic response of materials is described as $n = n_0 + n_2 I$, where n_0 is the linear refractive index and n_2 is the nonlinear refractive index. The change of refractive index due to light-matter interactions has enabled control of light in the spatial and frequency domains,[1] and created numerous applications such as optical switching,[2,3] ultrafast pulse generation,[4] and solitons.[5] Although nonresonant-type optical nonlinearity is often an inherently weak effect, artificial metamaterials can significantly enhance the effective nonlinear response at subwavelength scales due to resonant light−matter interactions.[6−12] Emerging plasmonic materials such as transparent conducting oxides (TCOs)[13,14] have been shown to exhibit large optical nonlinearities arising from free carrier behaviors that can be tuned by resonant optical pumping.[15−19] However, the large nonlinear response of TCOs achieved in the ε-near-zero[20] to the metallic range (primarily in the near- to mid-infrared) comes with a price of intrinsic material loss, which may ultimately limit the efficiency of desired optical functions. The transparent semiconducting oxide (TSO) counterparts of TCOs, which have been deployed in next-generation optoelectronic devices,[21] represent another class of potential nonlinear optical materials. For example, indium oxide (IO), the TSO version of ITO, is transparent from the visible to the infrared with a direct bandgap in the ultraviolet (UV).[22,23] The unique electronic configuration of IO lends itself to strong redistributions of valence electrons under readily accessible UV pumping, which in turn may largely impact its optical response. Here we demonstrate large negative optical nonlinearity of IO arranged in periodic nanorod array structures. Interband optical excitation transiently photodope indium oxide nanorod arrays (IO-NRAs), resulting in a reduction of the real component of refractive index without introducing any additional loss into the full-visible range.

RESULTS AND DISCUSSION

Periodic, vertically aligned IO-NRAs were grown via the vapor−liquid−solid mechanism (see Supporting Information, Section 1, and Figure S1). A scanning electron micrograph of the IO-NRA with height, pitch size, and average edge length of 2.55 μm, 1 μm, and 180 nm is shown in Figure 1a. The single-crystalline IO-NRAs were epitaxially grown on lattice-matched yttria-stabilized-zirconia substrates along the [001] direction (see Figure S2). Figure 1b shows the visible transmission spectrum. Five transmission dips, centered at 691, 541, 468, 424, and 393 nm, arise from the destructive interference between light propagating in nanorods and in free space, where

Received: March 19, 2017

DOI: 10.1021/acsphotonics.7b00278
ACS Photonics XXXX, XXX, XXX−XXX

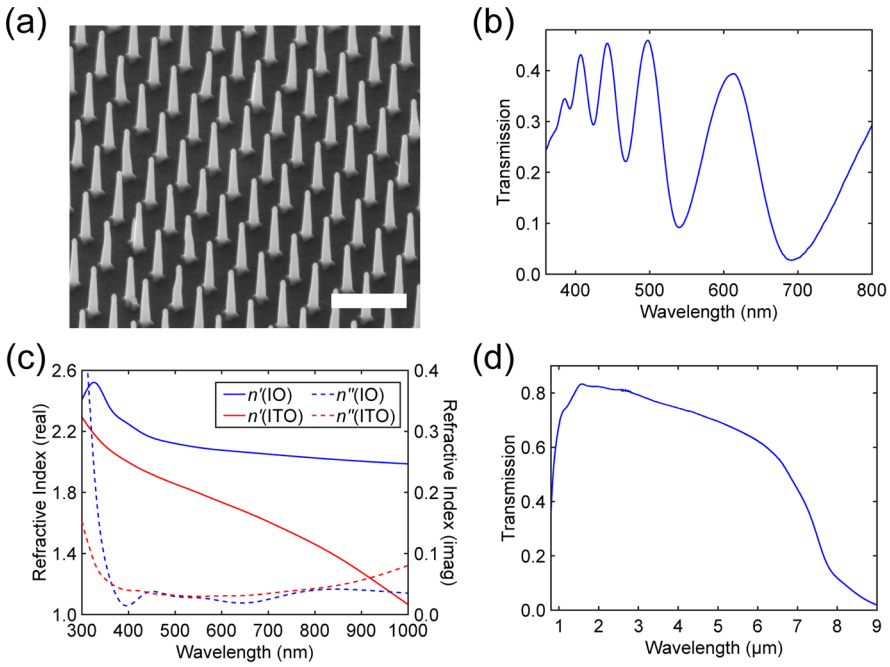

Figure 1. Static optical properties of the IO-NRA. (a) Scanning electron micrograph of the IO-NRA under 30° viewing angle (scale bar: 2 μm). (b) Visible transmission spectrum of the IO-NRA. (c) $n'(\omega)$ and $n''(\omega)$ of epitaxial IO and ITO films obtained from ellipsometric measurements. (d) Infrared transmission spectrum of the IO-NRA. Both (b) and (d) are taken at normal incidence and referenced to air.

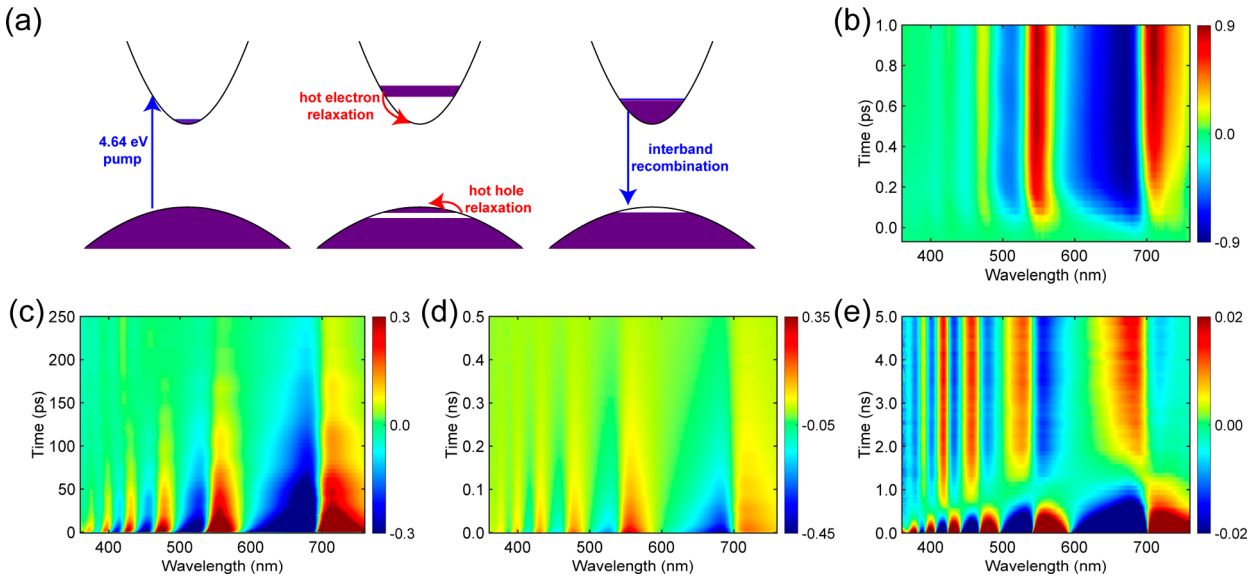

Figure 2. Transient optical response. (a) Schematic drawing of the electronic processes following the 267 nm pump excitation. (b−e) $\Delta T/T$ transient spectral maps for delay time windows up to 1 ps, 250 ps, 0.5 ns, and 5 ns, respectively. Pump fluences from (b) to (e) are 6.45, 4.44, 1.12, and 1.12 mJ·cm^{-2}.

the dielectric array behaves as a two-dimensional optical grating.[24,25] Various higher diffraction orders were produced by the nanorod array; here, in both the static and time-resolved experiments, we only collected the (0, 0) order. Similar to the ITO nanorod array case, at the transmission minima of the (0, 0) order shown in Figure 1b, diffraction into the higher orders is maximized, which corresponds to an out-of-phase condition for waves propagating inside the IO nanorod and in air.[24,25] Note that the reddest dip at 691 nm is ∼100 nm redder than that observed for ITO-NRA with similar dimensions;[24] this difference originates from a higher refractive index of IO and with it a larger difference of optical path lengths between waves propagating in the nanorods and in free space. Figure 1c depicts the real and imaginary components of the refractive index, denoted as $n'(\omega)$ and $n''(\omega)$, for both IO and ITO obtained from ellipsometric measurements on respective epitaxial thin films sputtered on YSZ substrates; these films share the same single-crystalline quality as the nanorod counterparts (see Supporting Information, Section 2). IO and ITO have comparably low $n''(\omega)$ in most of the visible range, except that the absorption onset of IO is at ∼400 nm, slightly redder than ITO at ∼370 nm. An overall weaker transmission intensity of IO-NRA compared to the ITO counterpart is likely attributed to a less ideal uniformity of the former. A larger

DOI: 10.1021/acsphotonics.7b00278
ACS Photonics XXXX, XXX, XXX−XXX

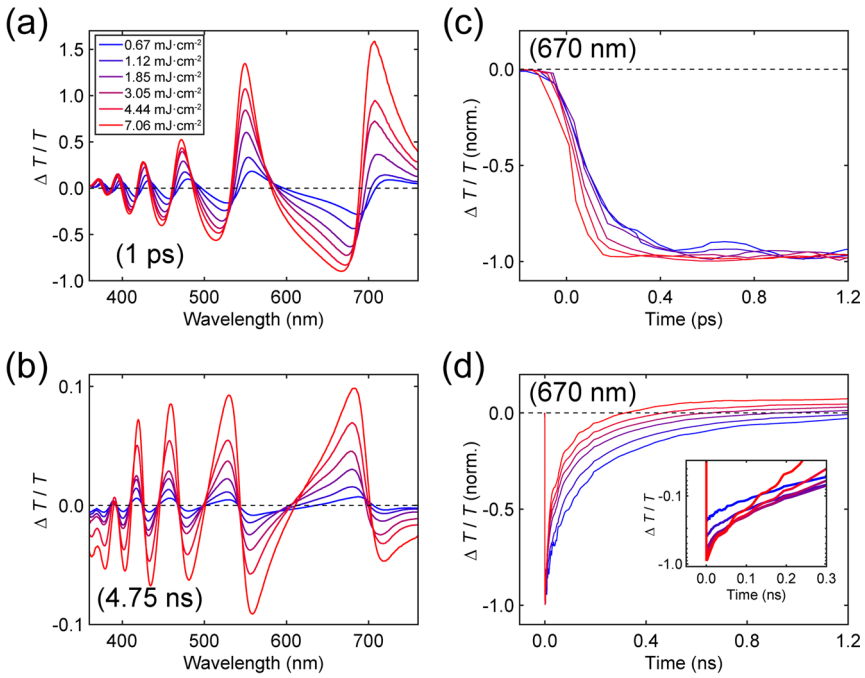

Figure 3. Fluence dependent transient responses. (a and b) Fluence-dependent $\Delta T/T$ spectra at 1 ps and 4.75 ns delay time, respectively. (c and d) Fluence-dependent, normalized $\Delta T/T$ kinetics (at 670 nm) up to 1.2 ps and 1.2 ns, respectively. Inset of (d) shows actual values of $\Delta T/T$ in log scale for the first 0.3 ns. Legend in (a) applies to all panels.

$n'(\omega)$ of IO arises owing to (1) The high density of conduction electrons (denoted as n) in ITO yields to a plasma frequency (ω_p) close to 2 eV,[17] which, according to the Drude relative permittivity, $\varepsilon(\omega) = \varepsilon_\infty - \omega_p^2/(\omega^2 + i\gamma_p\omega)$, leads to a reduction of $\varepsilon'(\omega)$ particularly in the near-infrared region. Here γ_p is the damping factor and $\varepsilon'(\omega)$ is the real part of the relative permittivity. (2) A smaller effective bandgap of IO due to the absence of Burstein−Moss effect[26] moves the onset of interband optical transition closer to the visible range, which yields a larger $\varepsilon'(\omega)$ especially near the UV. The absence of localized surface plasmon resonance (LSPR) up to 8 μm (the YSZ substrate becomes opaque at wavelengths redder than 7 μm) in the infrared transmission spectrum shown in Figure 1d suggests that n of the as-grown IO-NRA arising from native oxygen vacancies[27] is less than 5×10^{19} cm^{-3} (see Supporting Information, Section 3), which is at least 1 order of magnitude lower compared to ITO.

We performed pump−probe experiments on the IO-NRA. The sample was excited by 267 nm, 35 fs pulses and probed by broadband white light pulses (from 360 to 760 nm) under normal incidence. The 267 nm photons with energy (4.65 eV) larger than the effective bandgap of IO (3.5−3.7 eV)[28,29] can promote electrons from the valence band (VB) to the conduction band (CB), thereby transiently photodoping the material.[16,30] Here the effective bandgap of IO equals $E_g + \mu_0$, where E_g is the energy difference between the CB minimum (CBM) and the VB maximum (VBM) and μ_0 is the static electron chemical potential. The difference between the pump photon energy and effective bandgap indicates that photo-excited electrons initially occupy states well above the electron chemical potential (denoted as μ); the hot electrons and holes relax to lowest unoccupied states in their respective bands through carrier-phonon coupling, and then recombine. The sequence of optical excitation, hot carrier relaxation, and interband recombination are illustrated in Figure 2a. Figure 2b−e presents the transient spectral maps of $\Delta T/T$ for delay time windows up to 1 ps, 250 ps, 0.5 ns, and 5 ns, respectively. Transient response during the first 1 ps (Figure 2b) reveals that $\Delta T/T$ spectrally alternates between positive and negative values from 360 to 760 nm; here each zero-crossing-wavelength from a negative $\Delta T/T$ region to a redder and positive $\Delta T/T$ region matches a static transmission dip. This characteristic spectral line-shape is caused by a transient blueshift of transmission; note that this is distinctively different from the dynamic redshift of transmission observed for ITO-NRAs under intraband optical excitation.[24] While the spectral redshift in ITO-NRA was due to an increase of $n'(\omega)$, here the spectral blueshift in IO-NRA is assigned to a decrease of $n'(\omega)$, which corresponds to negative optical nonlinearity.

Figure 2b shows an increase of $\Delta T/T$ intensity accompanied by a slight blueshift of the zero-crossing-wavelengths during the first 250 fs. This subps blueshift of $\Delta T/T$ after the impulsive pump excitation is associated with hot carrier relaxation, following which the $\Delta T/T$ intensity stays nearly constant for the first 1 ps. Figure 2c and d show a decay rate of $\Delta T/T$ in the few-tens to few-hundred ps range, which we attribute to the interband recombination of thermalized, excess electron, and hole populations. The oscillation of $\Delta T/T$ signals in Figure 2c is indicative of coherent acoustic phonons; the fact that the coherent phonons started at early ps delay time supports the interpretation that the subps blueshift of $\Delta T/T$ arises from hot carrier relaxation, as the cooling of hot carriers leads to an impulsive lattice heating and can initiate the acoustic phonon modes.[31,32] We can hence approximately treat the photoexcited electrons and holes after 0.25 ps presented from Figure 2b−e as thermalized (Fermi−Dirac like) and in quasi-equilibrium with the lattice. Figure 2e shows that after electrons and holes recombine (by ∼1 ns), the $\Delta T/T$ signals undergo a switch of sign, which arises because the transient response without excess carriers is dominated by a thermo-optical effect due to a lattice

DOI: 10.1021/acsphotonics.7b00278
ACS Photonics XXXX, XXX, XXX−XXX

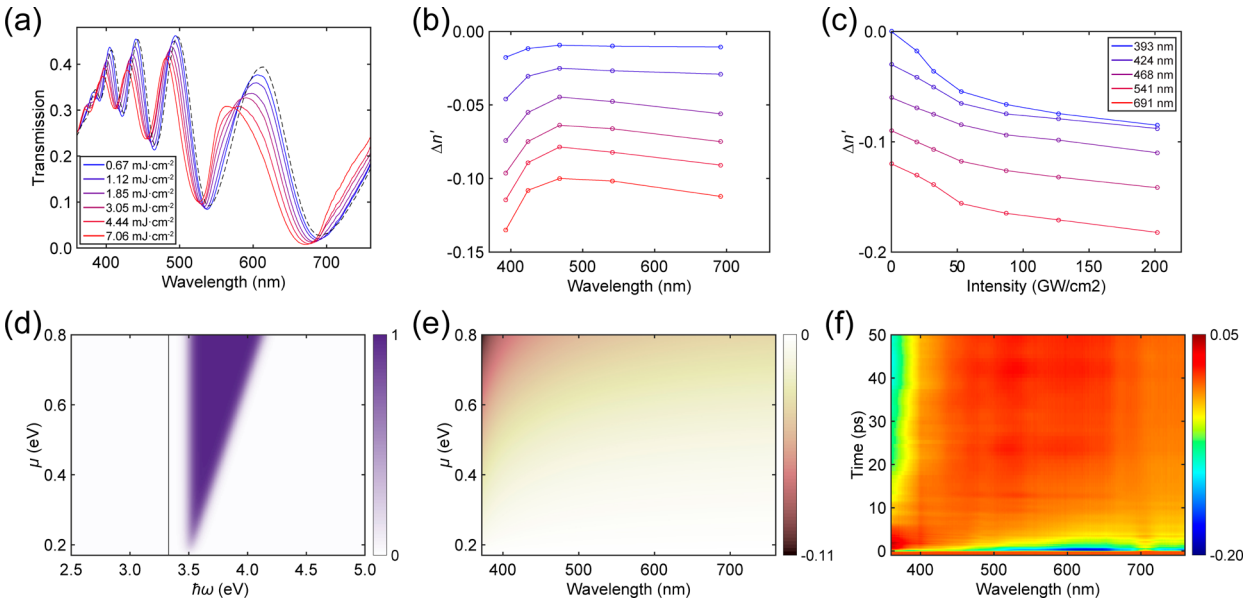

Figure 4. Quantification of the negative optical nonlinearity. (a) Fluence-dependent transmission spectra at 1 ps delay time. (b) Fluence-dependent $\Delta n'(\omega)$ at 1 ps delay time; each curve starting from 1.12 mJ·cm^{-2} is shifted in increments of −0.01 for clarity. Legend in (a) also applies to (b). (c) Intensity-dependent $\Delta n'(\omega)$ at 1 ps delay time for wavelengths of the static transmission dips; each curve starting from 424 nm is shifted in increments of −0.03 for clarity. (d) Change of electron occupation vs $\hbar\omega$ and μ. (e) Calculated $\Delta n'(\omega)$ vs wavelength and μ (referenced to CBM). (f) $\Delta T/T$ transient spectra of 220 nm thick epitaxial IO film under fluence of 6.59 mJ·cm^{-2}.

temperature rise. A decrease of bandgap at high lattice temperature[33] leads to a positive $\Delta n'(\omega)$ and with it a transmission redshift;[24] this is in contrast to the transient blueshift associated with a negative $\Delta n'(\omega)$ owing to excess carriers. Although the thermo-optical effect is expected to play a role immediately following the subps hot carrier relaxation, it is much less significant than the effect of photodoping, which is evident from the 1 order of magnitude larger $\Delta T/T$ amplitude in the ps range compared to that in the ns range. Figure 2e further shows that hot lattice induced $\Delta T/T$ exhibits no distinguishable decay up to 5 ns, suggesting that heat transfer in these large aspect-ratio structures with relatively low thermal conductivity[34] (a few W·m^{-1}·K^{-1}) takes place over μs time scales.[24]

Figure 3a presents the fluence dependent $\Delta T/T$ spectra at 1 ps delay time when photoexcited carriers are thermalized. We find a monotonic increase of $\Delta T/T$ amplitude under an increasing fluence. Remarkable differential suppression (enhancement) of transmission up to −90% (150%) is obtained at the highest fluence of 7.06 mJ·cm^{-2}. Fluence above 8 mJ·cm^{-2} resulted in irreversible loss of $\Delta T/T$ signals within minutes likely due to sample damage. Measurements on additional IO-NRAs show that differential modulation of transmission larger than 1000% can be achieved for particular spectral regions using long IO-NRAs (see Supporting Information, Section 4), which support large numbers of transmission dips and concomitantly large slopes in the transmission curve. The fluence dependent $\Delta T/T$ spectra at 4.75 ns, when hot lattice effects dominate, are presented in Figure 3b; these spectra exhibit opposite sign compared to those appearing in Figure 3a. Negative $\Delta T/T$ amplitude is observed for the spectral range below 390 nm, likely caused by depopulation of shallow trap states[35] at elevated lattice temperature, which can lead to below-bandgap absorption.

Figure 3c presents the fluence-dependent $\Delta T/T$ kinetics at 670 nm up to 1.2 ps; the subps rise time (hot carrier relaxation) does not exhibit a strong fluence dependence. However, the subsequent nanosecond $\Delta T/T$ decay shown in Figure 3d due to carrier recombination displays a strong fluence dependence. In a direct-bandgap semiconductor such as IO, carrier recombination rate is generally written as $R = An + Bn^2 + Cn^3$, where An, Bn^2, and Cn^3 represent trap-assisted, radiative (band-to-band), and Auger recombination rates, respectively.[36] The strong dependence of recombination rate on fluence (and hence on $n(0)$, where $n(0)$ is the excess carrier concentration right after the pump excitation) suggests that higher order processes (Bn^2 and Cn^3 terms) contribute to the carrier recombination in addition to trap-assisted processes. Note that trap-assisted process alone would yield a fixed decay constant (dependent on A but not on $n(0)$). Time-resolved photoluminescence spectra shown in Supporting Information, Figure S10, demonstrate both band-to-band emission below 400 nm, and trap-assisted emission from 400 to 650 nm. Consistent with the interpretation of the fluence dependent $\Delta T/T$ decay rates, faster photoluminescence kinetics and stronger band-to-band radiation are obtained under higher excitation fluence. This is in sharp contrast to heavily doped TCOs such as ITO[30] or aluminum doped zinc oxide (AZO),[16] where high doping concentration of foreign atoms (on the order of 10%) yields ultrafast trap-assisted recombination in the sub- to single-digit ps regime. The few-hundred-ps recombination rate in IO is however faster than in other direct-bandgap semiconductors such as GaAs[37] and CdSe,[38] hence both radiative and Auger recombination processes may contribute, given the large value of $n(0)$ reached in our experiments (as estimated when discussing Figure 4e in the second last paragraph before the conclusion).

We note that electron−phonon coupling[39] in IO can be assessed by temperature dependence of the initial $\Delta T/T$ blueshift associated with hot carrier relaxation. In Supporting Information, Figure S5, we show the $\Delta T/T$ spectral maps acquired at 150 and 3 K, respectively. At both temperatures the

DOI: 10.1021/acsphotonics.7b00278
ACS Photonics XXXX, XXX, XXX−XXX

subps $\Delta T/T$ blueshift exhibits similar time scales as compared to the room temperature counterpart (Figure 2b). The independence of hot carrier relaxation time on temperature suggests that scattering of electrons by defects (such as ionized impurities associated with oxygen vacancies) rather than by acoustic or optical phonons is the dominant mechanism of electron−phonon coupling in IO nanorods.[40]

The static and transient optical responses combined permit the estimation of the nonlinear refractive index change. Figure 4a shows the total transmission at 1 ps by adding the differential change of transmission (Figure 3a) and the static transmission (Figure 1b). The spectral shifts of the transmission dips permit the quantification of fluence and wavelength dependent $\Delta n'(\omega)$ (see Supporting Information, Section 6), which is shown in Figure 4b. We found that (1) $\Delta n'(\omega)$ peaks at the bluest dip wavelength of 393 nm. (2) At high fluences, the relative amplitude of $\Delta n'(\omega)$ at long wavelengths increases. (3) Large $\Delta n'(\omega)$ ranging from −0.05 to −0.09 is achieved at the maximal fluence of 7.06 mJ·cm^{-2}. The optical nonlinearity shown here significantly differs from recent results[15,17,41] on TCOs from three perspectives: (1) $\Delta n'(\omega)$ of IO due to a change of electron doping concentration is negative (pertaining to a negative optical nonlinearity), whereas $\Delta n'(\omega)$ in TCOs arising from a change of electron temperature was positive. (2) $\Delta n'(\omega)$ in TCOs was in the epsilon-near-zero (ENZ) to metallic regime, where materials can become lossy due to free carrier effects. $\Delta n'(\omega)$ shown here is in the transparent regime of IO. (3) The static $n'(\omega)$ of TCOs in the ENZ region is usually smaller than unity. Here the static $n'(\omega)$ ranges from 2 to 2.5, comparable to TiO_2, which was used for dielectric metasurfaces due to its high index and low loss.[42] We also note that metal-to-insulator transitions in correlated electron materials such as VO_2 can offer negative $\Delta n'(\omega)$ in the visible to infrared range,[43] but in that case a large $n''(\omega)$ of the metallic phase limits their use in nonlinear optical devices where loss is detrimental. Figure 4c shows the dependence of $\Delta n'(\omega)$ on the peak excitation power at different wavelengths. We note that intensity in the GW·cm^{-2} regime related to fs pump pulses can be easily reduced to the MW·cm^{-2} range by using ps pump pulses, which are still much shorter than the recovery time of the optical nonlinearity of IO. This indicates that the optical nonlinearity discussed here can be accessed by fiber lasers,[44] whereas achieving sub- to single-digit ps optical nonlinearity in TCOs requires fs laser/amplifier systems.

The negative optical nonlinearity of IO is attributed to a modification of interband optical transitions, which produces a positive change of $n''(\omega)$ at energies above the effective bandgap (in the UV). Photodoping by the interband pump effectively raises μ of the electrons. The effect of photodoping on holes in the VB is however much less significant, because of a much higher density of states for holes owing to the flat valence bands.[45] Dictated by the Kramers−Kronig (KK) relation which links the real and imaginary parts of frequency-dependent susceptibilities, the change of $n''(\omega)$ at above-bandgap energies results in a change of $n'(\omega)$ extended into the below-bandgap, full-visible range. The change of electron occupation is plotted in Figure 4d as a function of $\hbar\omega$ (photon energy) and μ. The carriers are assumed to be at 300 K, which is valid because lattice temperature rise (which equals the carrier temperature rise as hot carriers quickly relax to band edges) is at most a couple hundred Kelvin, which has a negligible impact on electron occupation in comparison to the photodoping effect that moves μ over hundreds of meV (much larger than k_BT at room temperature where k_B is the Boltzmann constant). The change of electron occupation permits the calculation of $\Delta n'(\omega)$, which is color-coded in Figure 4e. Details of the theoretical calculation appear in Supporting Information, Section 7. Due to the large electron concentration generated by photodoping, a nonparabolic band was assumed for the calculation of the change of μ and $n'(\omega)$.[46] Consistent with $\Delta n'(\omega)$ shown in Figure 4b deduced from experiments, $\Delta n'(\omega)$ displayed in Figure 4e is peaked at shorter wavelengths; this arises from the KK relation which dictates that $\Delta n'(\omega)$ is large around and vanishes away from the energy range where $\Delta n''(\omega)$ occurs. Comparing Figure 4e and b, we estimate that μ is raised by 0.4−0.6 eV (from 0.17 to 0.6−0.8 eV) under the highest fluence of 7.06 mJ·cm^{-2}. An excess electron concentration of 5−7 × 10^{20} cm^{-3} can be estimated under such change of μ (see Supporting Information, Figure S4). From the Drude permittivity, an increase of ω_p due to photodoping is expected to give another contribution to the reduction of $\varepsilon'(\omega)$ and may explain the rise of $\Delta n'(\omega)$ amplitude at long wavelengths under high fluences.

Finally, we comment on the advantage of the periodic nanorod arrays presented in this work. The multiple transmission dips supported by the dielectric nanorod array exhibit strong transient optical features, thereby permitting the quantification of $\Delta n'(\omega)$. A transient spectral map produced for a 220 nm thick epitaxial IO film (Figure 4f) does not provide information regarding the change of $n'(\omega)$, primarily due to a featureless transmission spectrum (Figure S10a). A bare YSZ substrate (see Supporting Information, Section 8) exhibits a negative $\Delta T/T$ with a characteristic decay time of 3 ps, which can contribute to the negative change of transmission in Figure 4f if the IO film does not fully absorb the pump photons; this adds complexity to the understanding the transient optical response of IO. The substrate response does not impact the interpretation of transient features of the IO-NRAs, as only the spectral shifts of transmission dips are taken into account to deduce the optical nonlinearity.

■ CONCLUSION

In summary, we demonstrate that large negative optical nonlinearity can be realized by interband optical pumping of a direct bandgap semiconductor, here exemplified by IO-NRA. The prominent spectral features of the dielectric nanorod array allow the separation of carrier cooling, recombination, and hot lattice effects. Although carrier dynamics of various wide-bandgap semiconductors have been studied,[47,48] here we quantify the change of refractive index as a function of pump fluence, and theoretically show that the negative optical nonlinearity derives from a strong modification of above-bandgap optical transitions. Although the demonstrated modulation scheme can be achieved with other direct bandgap semiconductors, the large bandgap of IO leads to negative optical nonlinearity in the full-visible spectral range without increasing the loss. This is to be compared to semiconductors with bandgaps located in the visible range (such as GaAs, InP, which exhibit loss in the visible) or in the deep UV (such as BN, AlN, which cannot offer large index modulation in the visible). The large negative optical nonlinearity in TSOs in conjunction with their versatile electrical properties may find applications in dynamically tunable subwavelength dielectric metasurfaces,[49] and in nonlinear nano-optics and active plasmonics when IO is interfaced with metallic components.

DOI: 10.1021/acsphotonics.7b00278
ACS Photonics XXXX, XXX, XXX−XXX

■ ASSOCIATED CONTENT

Supporting Information

The Supporting Information is available free of charge on the ACS Publications website at DOI: 10.1021/acsphotonics.7b00278.

Additional information about the fabrication of the nanorod arrays, optical characterization, fitting of the optical constants, transient absorption data, and discussion on the theoretical modeling (PDF).

■ AUTHOR INFORMATION

Corresponding Authors

*E-mail: r-chang@northwestern.edu.

*E-mail: schaller@anl.gov; schaller@northwestern.edu.

ORCID

Peijun Guo: 0000-0001-5732-7061

Richard D. Schaller: 0000-0001-9696-8830

Notes

The authors declare no competing financial interest.

■ ACKNOWLEDGMENTS

This work was performed, in part, at the Center for Nanoscale Materials, a U.S. Department of Energy, Office of Science, Office of Basic Energy Sciences User Facility under Contract No. DE-AC02-06CH11357. P.G. and R.P.H.C. acknowledge the MRSEC Program (NSF DMR-1121262) at Northwestern University.

■ REFERENCES

(1) Boyd, R. W. *Nonlinear Opt.*, 3rd ed.; Academic Press, 2008.

(2) MacDonald, K. F.; Samson, Z. L.; Stockman, M. I.; Zheludev, N. I. Ultrafast Active Plasmonics. *Nat. Photonics* **2009**, *3*, 55−58.

(3) Shcherbakov, M. R.; Vabishchevich, P. P.; Shorokhov, A. S.; Chong, K. E.; Choi, D.-Y.; Staude, I.; Miroshnichenko, A. E.; Neshev, D. N.; Fedyanin, A. A.; Kivshar, Y. S. Ultrafast All-Optical Switching with Magnetic Resonances in Nonlinear Dielectric Nanostructures. *Nano Lett.* **2015**, *15*, 6985−6990.

(4) Cerullo, G.; De Silvestri, S.; Magni, V. Self-Starting Kerr-Lens Mode Locking of a Ti:Sapphire Laser. *Opt. Lett.* **1994**, *19*, 1040−1042.

(5) Leo, F.; Coen, S.; Kockaert, P.; Gorza, S.-P.; Emplit, P.; Haelterman, M. Temporal Cavity Solitons in One-Dimensional Kerr Media as Bits in an All-Optical Buffer. *Nat. Photonics* **2010**, *4*, 471−476.

(6) Lee, J.; Tymchenko, M.; Argyropoulos, C.; Chen, P.-Y.; Lu, F.; Demmerle, F.; Boehm, G.; Amann, M.-C.; Alu, A.; Belkin, M. A. Giant Nonlinear Response from Plasmonic Metasurfaces Coupled to Intersubband Transitions. *Nature* **2014**, *511*, 65−69.

(7) Kauranen, M.; Zayats, A. V. Nonlinear Plasmonics. *Nat. Photonics* **2012**, *6*, 737−748.

(8) Renger, J.; Quidant, R.; van Hulst, N.; Novotny, L. Surface-Enhanced Nonlinear Four-Wave Mixing. *Phys. Rev. Lett.* **2010**, *104*, 046803.

(9) Aouani, H.; Rahmani, M.; Navarro-Cia, M.; Maier, S. A. Third-Harmonic-Upconversion Enhancement from a Single Semiconductor Nanoparticle Coupled to a Plasmonic Antenna. *Nat. Nanotechnol.* **2014**, *9*, 290−294.

(10) O'Brien, K.; Suchowski, H.; Rho, J.; Salandrino, A.; Kante, B.; Yin, X.; Zhang, X. Predicting Nonlinear Properties of Metamaterials from the Linear Response. *Nat. Mater.* **2015**, *14*, 379−383.

(11) Utikal, T.; Zentgraf, T.; Paul, T.; Rockstuhl, C.; Lederer, F.; Lippitz, M.; Giessen, H. Towards the Origin of the Nonlinear Response in Hybrid Plasmonic Systems. *Phys. Rev. Lett.* **2011**, *106*, 133901.

(12) Vallée, F., Ultrafast Non-Equilibrium Electron Dynamics in Metal Nanoparticles. In *Non-Equilibrium Dynamics of Semiconductors and Nanostructures*; Tsen, K.-T., Ed.; Taylor & Francis Group: Boca Raton, FL, 2005.

(13) Boltasseva, A.; Atwater, H. A. Low-Loss Plasmonic Metamaterials. *Science* **2011**, *331*, 290−291.

(14) Naik, G. V.; Liu, J.; Kildishev, A. V.; Shalaev, V. M.; Boltasseva, A. Demonstration of Al:ZnO as a Plasmonic Component for Near-Infrared Metamaterials. *Proc. Natl. Acad. Sci. U. S. A.* **2012**, *109*, 8834−8838.

(15) Alam, M. Z.; De Leon, I.; Boyd, R. W. Large Optical Nonlinearity of Indium Tin Oxide in its Epsilon-Near-Zero Region. *Science* **2016**, *352*, 795−797.

(16) Kinsey, N.; DeVault, C.; Kim, J.; Ferrera, M.; Shalaev, V. M.; Boltasseva, A. Epsilon-Near-Zero Al-doped ZnO for Ultrafast Switching at Telecom Wavelengths. *Optica* **2015**, *2*, 616−622.

(17) Guo, P.; Schaller, R. D.; Ketterson, J. B.; Chang, R. P. H. Ultrafast Switching of Tunable Infrared Plasmons in Indium Tin Oxide Nanorod Arrays with Large Absolute Amplitude. *Nat. Photonics* **2016**, *10*, 267−273.

(18) Abb, M.; Wang, Y.; de Groot, C. H.; Muskens, O. L. Hotspot-Mediated Ultrafast Nonlinear Control of Multifrequency Plasmonic Nanoantennas. *Nat. Commun.* **2014**, *5*, 4869.

(19) Capretti, A.; Wang, Y.; Engheta, N.; Dal Negro, L. Comparative Study of Second-Harmonic Generation from Epsilon-Near-Zero Indium Tin Oxide and Titanium Nitride Nanolayers Excited in the Near-Infrared Spectral Range. *ACS Photonics* **2015**, *2*, 1584−1591.

(20) Alù, A.; Silveirinha, M. G.; Salandrino, A.; Engheta, N. Epsilon-Near-Zero Metamaterials and Electromagnetic Sources: Tailoring the Radiation Phase Pattern. *Phys. Rev. B: Condens. Matter Mater. Phys.* **2007**, *75*, 155410.

(21) Yu, X.; Marks, T. J.; Facchetti, A. Metal Oxides for Optoelectronic Applications. *Nat. Mater.* **2016**, *15*, 383−396.

(22) Oliver, B. Indium Oxide—a Transparent, Wide-Band Gap Semiconductor for (Opto)Electronic Applications. *Semicond. Sci. Technol.* **2015**, *30*, 024001.

(23) Walsh, A.; Da Silva, J. L. F.; Wei, S.-H.; Körber, C.; Klein, A.; Piper, L. F. J.; DeMasi, A.; Smith, K. E.; Panaccione, G.; Torelli, P.; Payne, D. J.; Bourlange, A.; Egdell, R. G. Nature of the Band Gap of In_2O_3 Revealed by First-Principles Calculations and X-ray Spectroscopy. *Phys. Rev. Lett.* **2008**, *100*, 167402.

(24) Guo, P.; Schaller, R. D.; Ocola, L. E.; Diroll, B. T.; Ketterson, J. B.; Chang, R. P. H. Large Optical Nonlinearity of ITO Nanorods for Sub-Picosecond All-Optical Modulation of the Full-Visible Spectrum. *Nat. Commun.* **2016**, *7*, 12892.

(25) Li, S.-Q.; Sakoda, K.; Ketterson, J. B.; Chang, R. P. H. Broadband Resonances in Indium-Tin-Oxide Nanorod Arrays. *Appl. Phys. Lett.* **2015**, *107*, 031104.

(26) Hamberg, I.; Granqvist, C. G.; Berggren, K. F.; Sernelius, B. E.; Engström, L. Band-Gap Widening in Heavily Sn-doped In_2O_3. *Phys. Rev. B: Condens. Matter Mater. Phys.* **1984**, *30*, 3240−3249.

(27) Preissler, N.; Bierwagen, O.; Ramu, A. T.; Speck, J. S. Electrical Transport, Electrothermal Transport, and Effective Electron Mass in Single-Crystalline In_2O_3 Films. *Phys. Rev. B: Condens. Matter Mater. Phys.* **2013**, *88*, 085305.

(28) Weiher, R. L.; Ley, R. P. Optical Properties of Indium Oxide. *J. Appl. Phys.* **1966**, *37*, 299−302.

(29) Hamberg, I.; Granqvist, C. G. Evaporated Sn-doped In_2O_3 films: Basic Optical Properties and Applications to Energy-Efficient Windows. *J. Appl. Phys.* **1986**, *60*, R123−R160.

(30) Tice, D. B.; Li, S.-Q.; Tagliazucchi, M.; Buchholz, D. B.; Weiss, E. A.; Chang, R. P. H. Ultrafast Modulation of the Plasma Frequency of Vertically Aligned Indium Tin Oxide Rods. *Nano Lett.* **2014**, *14*, 1120−1126.

(31) Guo, P.; Schaller, R. D.; Ocola, L. E.; Ketterson, J. B.; Chang, R. P. H. Gigahertz Acoustic Vibrations of Elastically Anisotropic Indium−Tin-Oxide Nanorod Arrays. *Nano Lett.* **2016**, *16*, 5639−5646.

(32) Hartland, G. V. Optical Studies of Dynamics in Noble Metal Nanostructures. *Chem. Rev.* **2011**, *111*, 3858−3887.

DOI: 10.1021/acsphotonics.7b00278
ACS Photonics XXXX, XXX, XXX−XXX

(33) Wei, Z. P.; Guo, D. L.; Liu, B.; Chen, R.; Wong, L. M.; Yang, W. F.; Wang, S. J.; Sun, H. D.; Wu, T. Ultraviolet Light Emission and Excitonic Fine Structures in Ultrathin Single-Crystalline Indium Oxide Nanowires. *Appl. Phys. Lett.* **2010**, *96*, 031902.

(34) Ashida, T.; Miyamura, A.; Oka, N.; Sato, Y.; Yagi, T.; Taketoshi, N.; Baba, T.; Shigesato, Y. Thermal Transport Properties of Polycrystalline Tin-Doped Indium Oxide Films. *J. Appl. Phys.* **2009**, *105*, 073709.

(35) Liang, C. H.; Meng, G. W.; Lei, Y.; Phillipp, F.; Zhang, L. D. Catalytic Growth of Semiconducting In_2O_3 Nanofibers. *Adv. Mater.* **2001**, *13*, 1330−1333.

(36) Coldren, L. A.; Corzine, S. W.; Mašanović, M. L. *Diode Lasers and Photonic Integrated Circuits*; John Wiley & Sons: Hoboken, NJ, 2012.

(37) Boland, J. L.; Casadei, A.; Tütüncüoglu, G.; Matteini, F.; Davies, C. L.; Jabeen, F.; Joyce, H. J.; Herz, L. M.; Fontcuberta i Morral, A.; Johnston, M. B. Increased Photoconductivity Lifetime in GaAs Nanowires by Controlled n-Type and p-Type Doping. *ACS Nano* **2016**, *10*, 4219−4227.

(38) Nair, G.; Bawendi, M. G. Carrier Multiplication Yields of CdSe and CdTe Nanocrystals by Transient Photoluminescence Spectroscopy. *Phys. Rev. B: Condens. Matter Mater. Phys.* **2007**, *76*, 081304.

(39) Wright, A. D.; Verdi, C.; Milot, R. L.; Eperon, G. E.; Pérez-Osorio, M. A.; Snaith, H. J.; Giustino, F.; Johnston, M. B.; Herz, L. M. Electron−Phonon Coupling in Hybrid Lead Halide Perovskites. *Nat. Commun.* **2016**, *7*, 11755.

(40) Rudin, S.; Reinecke, T. L.; Segall, B. Temperature-Dependent Exciton Linewidths in Semiconductors. *Phys. Rev. B: Condens. Matter Mater. Phys.* **1990**, *42*, 11218−11231.

(41) Caspani, L.; Kaipurath, R. P. M.; Clerici, M.; Ferrera, M.; Roger, T.; Kim, J.; Kinsey, N.; Pietrzyk, M.; Di Falco, A.; Shalaev, V. M.; Boltasseva, A.; Faccio, D. Enhanced Nonlinear Refractive Index in ε-Near-Zero Materials. *Phys. Rev. Lett.* **2016**, *116*, 233901.

(42) Khorasaninejad, M.; Chen, W. T.; Devlin, R. C.; Oh, J.; Zhu, A. Y.; Capasso, F. Metalenses at Visible Wavelengths: Diffraction-Limited Focusing and Subwavelength Resolution Imaging. *Science* **2016**, *352*, 1190−1194.

(43) Briggs, R. M.; Pryce, I. M.; Atwater, H. A. Compact Silicon Photonic Waveguide Modulator based on the Vanadium Dioxide Metal-Insulator Phase Transition. *Opt. Express* **2010**, *18*, 11192−11201.

(44) Muskens, O. L.; Bergamini, L.; Wang, Y.; Gaskell, J. M.; Zabala, N.; de Groot, C. H.; Sheel, D. W.; Aizpurua, J. Antenna-Assisted Picosecond Control of Nanoscale Phase Transition in Vanadium Dioxide. *Light: Sci. Appl.* **2016**, *5*, e16173.

(45) Mryasov, O. N.; Freeman, A. J. Electronic Band Structure of Indium Tin Oxide and Criteria for Transparent Conducting Behavior. *Phys. Rev. B: Condens. Matter Mater. Phys.* **2001**, *64*, 233111.

(46) Liu, X.; Park, J.; Kang, J.-H.; Yuan, H.; Cui, Y.; Hwang, H. Y.; Brongersma, M. L. Quantification and Impact of Nonparabolicity of the Conduction Band of Indium Tin Oxide on its Plasmonic Properties. *Appl. Phys. Lett.* **2014**, *105*, 181117.

(47) Johnson, J. C.; Knutsen, K. P.; Yan, H.; Law, M.; Zhang, Y.; Yang, P.; Saykally, R. J. Ultrafast Carrier Dynamics in Single ZnO Nanowire and Nanoribbon Lasers. *Nano Lett.* **2004**, *4*, 197−204.

(48) Tian, L.; di Mario, L.; Zannier, V.; Catone, D.; Colonna, S.; O'Keeffe, P.; Turchini, S.; Zema, N.; Rubini, S.; Martelli, F. Ultrafast carrier dynamics, band-gap renormalization, and optical properties of ZnSe nanowires. *Phys. Rev. B: Condens. Matter Mater. Phys.* **2016**, *94*, 165442.

(49) Huang, Y.-W.; Lee, H. W. H.; Sokhoyan, R.; Pala, R. A.; Thyagarajan, K.; Han, S.; Tsai, D. P.; Atwater, H. A. Gate-Tunable Conducting Oxide Metasurfaces. *Nano Lett.* **2016**, *16*, 5319−5325.

DOI: 10.1021/acsphotonics.7b00278
ACS Photonics XXXX, XXX, XXX−XXX